



# Electron-enriched supramolecular PDI-SiO<sub>2</sub> promoting PDS activation for enhanced photocatalytic advanced oxidation

Wenting Li<sup>a</sup>, Hanjie Zhang<sup>b</sup>, Sijie Huang<sup>a</sup>, Jingyi Xu<sup>a</sup>, Liping Liu<sup>a</sup>, Junshan Li<sup>d</sup>,  
Jianfang Jing<sup>c,\*</sup>, Yongfa Zhu<sup>a,\*</sup>

<sup>a</sup> Department of Chemistry, Tsinghua University, Beijing 100084, PR China

<sup>b</sup> Beijing Key Laboratory of Research and Application for Aerospace Green Propellants, Beijing Institute of Aerospace Testing Technology, Beijing 100074, PR China

<sup>c</sup> College of Chemistry and Chemical Engineering, Inner Mongolia University, Hohhot 010021, PR China

<sup>d</sup> Institute for Advanced Study, Chengdu University, Chengdu 610106, PR China

## ARTICLE INFO

### Keywords:

Photocatalytic  
Advanced oxidation  
PDS activation  
Mineralization

## ABSTRACT

The efficient activation of peroxydisulfate (PDS) for wastewater treatment remains a great challenge. Photocatalysis, which generates highly-reactive electrons and holes, shows great potential in activating PDS for effective degradation and deep mineralization. Herein, an electron-enriched PDI-SiO<sub>2</sub> photocatalyst was synthesized by covalently linking 3,4,9,10-perylene tetracarboxylic dianhydride (PTCDA) onto silicon dioxide (SiO<sub>2</sub>) to form  $\pi$ - $\pi$  stacked supramolecular PDI layers for efficient PDS activation. The highly dispersed PDI generates electron-enriched PDI<sup>-</sup> under visible light, promoting the rapid activation of PDS for bisphenol A (BPA) degradation. The PDI-SiO<sub>2</sub> activated PDS system realized a high BPA degradation rate of 0.100 min<sup>-1</sup> and a remarkable mineralization rate of 81%. Moreover, the charge separation efficiency is significantly improved since the electrons of PDI<sup>-</sup> are captured by PDS, boosting oxidative degradation and improving the mineralization efficiency. This work developed a novel PDS activation strategy by constructing electron-enriched photocatalyst, and revealed the mechanism of photocatalytic activation and deep mineralization.

## 1. Introduction

Advanced oxidation process (AOPs) [1] characterized by the production of strong oxidizing free radicals is considered as a promising and effective organic wastewater treatment [2–4]. Compared with the Fenton reaction AOPs dominated by hydroxyl radical ( $\cdot$ OH) [5], activating persulfate (peroxymonosulfate (PMS) or peroxydisulfate (PDS)) to produce sulfate radical ( $\text{SO}_4^{\cdot-}$ ) has higher oxidation potential [6], more active radicals [7,8], longer half-life [9,10], and wider tolerance to environmental parameters (pH, peroxide concentration, etc.) [2,11,12]. However, due to the high stability of PDS in water, persulfate-based AOPs has low efficiency in decomposing organic pollutants [13]. In this case, many methods have been developed to activate PDS, including thermal activation [14,15], alkali activation [16,17], radiation activation [18–20], metal activation [21,22] and photocatalytic activation [23–26], among which photocatalytic activated PDS has attracted increasing attention due to its advantages of environmental friendliness, low cost and high efficiency electron transport.

Photocatalytic PDS activation for effective advanced oxidation

depends on the design of an excellent photocatalyst. Generally, the photocatalytic performance of materials can be significantly improved by increasing the specific surface area of the photocatalyst [27,28], promoting the migration of photogenerated electrons [29–31] and improving the utilization of visible light [26,32]. Inorganic photocatalysts are limited in activating persulfate due to the narrow spectrum response range, difficulty in regulating band structure and secondary pollution caused by metals [33–37]. In contrast, organic photocatalysts such as graphitic phase carbon nitride (g-C<sub>3</sub>N<sub>4</sub>) [23], metal organic frameworks (MOFs) [38], covalent organic frameworks (COFs) [39], conjugated organic polymers (COPs) [40], have attracted more attention in activating persulfate due to the advantages of wide spectral response, easy surface functional modification, tunable photoelectric properties, high mineralization rate, safety and economy.

Perylene diimide (PDI) and its derivatives were usually prepared by 3,4,9,10-perylene tetracarboxylic dianhydride (PTCDA) through condensation reaction with various amines, which had great potential for photocatalytic degradation of pollutants due to its excellent photo-transmission, visible light response and mechanical stability [41].

\* Corresponding authors.

E-mail addresses: [jingjf@imu.edu.cn](mailto:jingjf@imu.edu.cn) (J. Jing), [zhuyf@tsinghua.edu.cn](mailto:zhuyf@tsinghua.edu.cn) (Y. Zhu).

<https://doi.org/10.1016/j.apcatb.2023.123262>

Received 26 June 2023; Received in revised form 20 August 2023; Accepted 2 September 2023

Available online 4 September 2023

0926-3373/© 2023 Elsevier B.V. All rights reserved.

However, the low degradation rate and difficult mineralization greatly limit the application of PDI-based materials in photocatalytic advanced oxidation based on persulfate activation. PDI have been modified through reasonable strategies, such as functional group modification [42], supramolecular self-assembly [30], and heterojunction construction [24,29]. However, the insufficient active sites and severe recombination of photogenerated electrons and holes are still key scientific problems for efficient activation of PDS.

Herein, the electron-enriched PDI-SiO<sub>2</sub> photocatalyst was designed for rapid PDS activation to achieve enhanced photocatalytic advanced oxidation. PTCDA were covalently bonded to the surface of SiO<sub>2</sub> nanoparticles and self-assembled to a highly dispersed  $\pi$ - $\pi$  stacked supramolecular layer. This highly dispersed PDI-SiO<sub>2</sub> would increase surface interaction sites for PDS and pollutants, and shorten charge migration distance. Furthermore, supramolecular PDI-SiO<sub>2</sub> could produce electron-enriched anion radical PDI<sup>•-</sup> under visible light irradiation, whose electrons could be subsequently captured by PDS to achieve efficient and rapid activation of PDS. At the same time, the transfer of photogenerated electrons to PDS would enhance the separation and migration of photogenerated charge carriers, thereby promoting the participation of holes in oxidative degradation reactions. In this PDI-SiO<sub>2</sub>-activated PDS system, it is expected to achieve efficient degradation and deep mineralization of organic pollutants through cooperative effect of various reactive species, including SO<sub>4</sub><sup>•-</sup>, •OH, •O<sub>2</sub><sup>-</sup> and h<sup>+</sup>. This PDI-SiO<sub>2</sub> photocatalyst with multiple active sites and high charge separation efficiency provides a promising approach for efficient photocatalytic activation of PDS, which has potential industrial application in the field of visible light catalytic advanced oxidation.

## 2. Experimental section

### 2.1. Materials

All chemicals are analytically pure and require no further purification when used. Tetraethoxysilane (TEOS) and 3-amino-propyl triethoxysilane (APTES) were purchased from Beijing Chemical Works, 3,4,9,10-perylene tetracarboxylic dianhydride (PTCDA) was purchased from Energy Chemical, perylene diimide (PDINH), 3-aminopropionic acid and imidazole were purchased from Aladdin.

### 2.2. Preparation of PDI-based photocatalyst

#### 2.2.1. Preparation of PDI-SiO<sub>2</sub>

The PDI-SiO<sub>2</sub> was prepared by a two-step method (Scheme 1) [43]. Firstly, silica nanoparticles (SiO<sub>2</sub>-NH<sub>2</sub>) were prepared by hydrolysis of TEOS and APTES. Then, PTCDA were condensed with SiO<sub>2</sub>-NH<sub>2</sub> to afford PDI-SiO<sub>2</sub>.

(a) Preparation of SiO<sub>2</sub>-NH<sub>2</sub>: 8.44 g TEOS (40.5 mmol), 35.86 g

APTES (162 mmol) and 225 mL ethanol were added to 250 mL round-bottomed flask, heated to 65 °C and stirred for 10 min 8 mL water was added and the reaction mixture was stirred for 4.5 h. Afterwards, the mixture was cooled to room temperature, filtered by 0.45  $\mu$ m nylon membrane, washed with ethanol for three times, dried in vacuo at 120 °C for 12 h. Finally, white powder SiO<sub>2</sub>-NH<sub>2</sub> was afforded.

(b) Preparation of PDI-SiO<sub>2</sub>: 5 g imidazole, 0.7 g SiO<sub>2</sub>-NH<sub>2</sub> and 0.5 g PTCDA were added to a 100 mL round-bottomed flask, heated to 150 °C and stirred for 48 h. Afterwards, the reaction mixture was cooled to room temperature, added with the mixture of 50 mL ethanol and 30 mL 12 mol/L HCl, then transferred to a 250 mL beaker and stirred for another 10 h. The remaining PTCDA was removed by washing with 200 mL KOH (10 g/mL) and then KCl (10 g/mL) solution and filtration through a 0.45  $\mu$ m nylon membrane. The residual solid was neutralized with 1 mol/L HCl and dried in vacuo at 90 °C overnight to afford a dark brown powder as PDI-SiO<sub>2</sub>.

#### 2.2.2. Preparation of Self-assembled perylene diimide (PDINH)

Commercially available PDINH (1.00 g) was dispersed in concentrated H<sub>2</sub>SO<sub>4</sub> (100 mL) and sonicated for 10 min. Then the reaction mixture was quickly poured into deionized water (1000 mL). The suspension was filtered and rinsed with water to neutralize [44]. The residual solid was dried at 60 °C overnight to afford the self-assembled PDINH (0.90 g).

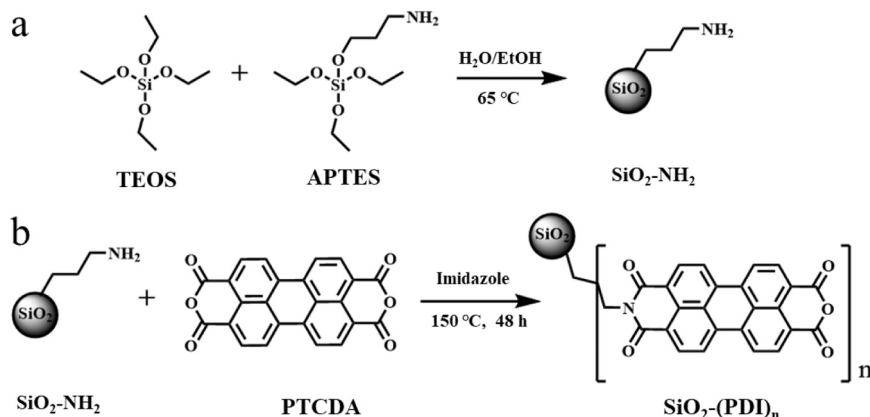
#### 2.2.3. Preparation of pure PDI

Similar to the above methods, commercially available PTCDA (1.00 g) was dispersed in concentrated H<sub>2</sub>SO<sub>4</sub> (100 mL) and sonicated for 10 min. Then the reaction mixture was quickly poured into deionized water (1000 mL). The suspension was filtered and rinsed with water to neutralize. The residual solid was dried at 60 °C overnight to afford the pure PDI.

#### 2.2.4. Preparation of Self-assembled Perylene diimide propionic acid (PDIPA)

Typically, 3.5 mmol PTCDA, 28.0 mmol 3-aminopropionic acid and 18 g imidazole were heated under argon at 100 °C for 4 h. The reaction mixture was cooled to room temperature and dispersed in 100 mL ethanol followed by addition of 300 mL 2.0 M HCl. The mixture was stirred overnight. The resulting red solid was collected by filtration through a 0.45  $\mu$ m membrane, and then washed thoroughly with distilled water until the pH turned to be neutral. The collected solid was dried in at 60 °C.

200.0 mL stock solution of N, N'-di(propionic acid)-perylene-3,4,9,10-tetracarboxylic diimide (5.0 mM) was prepared with addition of 834  $\mu$ L of TEA. The solution thus prepared looked clear, in red color. PDI nanofibers were formed by adding 27.3 mL 4.0 M HCl. It was washed thoroughly with distilled water until the pH of washings turned



**Scheme 1.** Synthetic route for PDI-SiO<sub>2</sub>. (a) Preparation of SiO<sub>2</sub>-NH<sub>2</sub>. (b) Preparation of PDI-SiO<sub>2</sub>.

to be neutral. The collected solid was dried in at 60 °C [45].

### 2.3. Characterization

Solid-state  $^{13}\text{C}$  nuclear magnetic resonance (NMR) spectra (150 MHz) were recorded with a JEOL JNM-ECZ600R spectrometer. Bruker V70 spectrometer was used for Fourier transform (FT)-infrared spectrum analysis. X-ray photoelectron spectroscopy (XPS) was recorded with a ThermoFisher ESCALAB 250Xi spectrometer. Transmission electron microscope (TEM) images were obtained using Hitachi HT7700 microscope. Scanning electron microscope (SEM) images were obtained on Hitachi SU8000 microscope. Ultraviolet-visible absorption spectra were recorded on Agilent Cary 5000 spectrophotometer. X-ray diffraction (XRD) patterns were recorded using Cu K $\alpha$  ( $\lambda = 0.154$  nm) on Rigaku (Smart-Lab) X-ray diffractometer. The Brunauer-Emmet-Teller (BET) specific surface area and pore distribution were measured using JWGB JW-BK200C isothermal nitrogen adsorption analyzer. Electron paramagnetic resonance (EPR) spectra were recorded on a JEOL FA-200 spectrometer using 5, 5-dimethyl-1-pyrroline-*N*-oxide (DMPO) as the spin trap. Surface photovoltage spectra were obtained on Zolix UOM-1S surface photovoltage spectrometer. Photocatalytic degradation reaction was carried out using XPA-7 parallel light reactor manufactured by Nanjing Xujiang Electrical Appliance Factory. The total organic carbon (TOC) was measured on a Jena Multi N/C 2100 TOC/TN spectrometer. Electrochemical measurements of photocatalysts were conducted using a CHI660E work station at room temperature in a 3-electrode cell, with Pt wire as the auxiliary electrode, saturated Ag/AgCl electrode as a reference, and NaCl aqueous solution (0.1 mol/L) as electrolyte. Working electrodes were prepared through dispersing samples (1.0 mg) in 2 mL deionized water by sonication for 10 min, coating the suspension on indium tin oxide (ITO) glass, drying at 60 °C overnight. A positive bias voltage of 0.2 V was provided in the electrochemical test.

### 2.4. Pollutant degradation measurement

The degradation experiment was conducted with 10 mg/L bisphenol A (BPA) as the target pollutant, 1 mmol/L PDS as the activated persulfate, and visible light ( $\lambda \geq 420$  nm) as the light source. The concentration of the pollutant BPA in the degraded solution was detected by high performance liquid chromatography (HPLC), and the mineralization rate was detected by total organic carbon (TOC) analyzer.

25 mg of PDI-SiO<sub>2</sub> and 44 mL of deionized water were added to quartz tube, then the photocatalyst was fully dispersed by ultrasound for 15 min. Add 5 mL BPA solution with a concentration of 100 mg/L, and stir in the dark for 30 min to reach adsorption-desorption equilibrium [46]. Then, add 1 mL of peroxydisulfate (PDS) solution with a concentration of 50 mmol/L, and remove 2 mL of suspension after mixing evenly. After the xenon lamp was illuminated to start the photocatalytic reaction, 2 mL of suspension was removed every 5 min until the reaction was over. The extracted solution was absorbed through a 2 mL syringe and then filtered through the syringe filter membrane to remove the catalyst. The filtered solution was used to detect the content of pollutants.

The degradation rate and TOC removal rate were evaluated using the formula in Eq. 1:

$$r = (c_0 - c)/c_0 \quad (1)$$

$r$  represents the degradation or TOC removal rate,  $c$  represents the detected concentration of BPA in the aliquot, and  $c_0$  represents the initial concentration of BPA.

### 2.5. Quenching experiments of reactive oxygen species

In the traditional photocatalytic degradation of pollutants, the main active species include photogenic holes ( $h^+$ ), hydroxyl radicals ( $\cdot\text{OH}$ ),

superoxide radicals ( $\cdot\text{O}_2^-$ ), etc. In the process of photocatalytic activation of PDS, sulfate radical ( $\text{SO}_4^{\cdot-}$ ) plays a key role as the main active species. To investigate the role of these active species in the photocatalytic activation of PDS by PDI-SiO<sub>2</sub> to degrade pollutants, we used BPA as the target pollutant to carry out the quenching experiment of active species. In the quenching experiment, methanol (MeOH) with concentration of 5 mmol/L was used as scavenger to quench sulfate radical ( $\text{SO}_4^{\cdot-}$ ) and hydroxyl radical ( $\cdot\text{OH}$ ), and tert-butanol (*t*-BuOH) with concentration of 5 mmol/L was used as scavenger to quench  $\cdot\text{OH}$ . 20 mmol/L formic acid (HCOOH) was used as a scavenger to quench photogenerated holes ( $h^+$ ), and 1 mmol/L *p*-benzoquinone (BQ) was used as a scavenger to quench superoxide radicals ( $\cdot\text{O}_2^-$ ). The contribution rate of each active species in degradation was calculated by Eq. 2:

$$R = \frac{k_{\text{app}} - k_r}{k_{\text{app}}} \quad (2)$$

$R$  (%) represents the contribution rate of the corresponding active species in the degradation system,  $k_{\text{app}}$  ( $\text{min}^{-1}$ ) represents the degradation rate constant without the scavenger, and  $k_r$  ( $\text{min}^{-1}$ ) represents the degradation rate constant after the addition of the corresponding scavenger.

## 3. Results and discussion

### 3.1. Covalently linked highly dispersed PDI-SiO<sub>2</sub> supermolecule

The chemical environment of C atoms in PDI-SiO<sub>2</sub> was characterized by  $^{13}\text{C}$  solid state nuclear magnetic resonance (SSNMR). As shown in Fig. 1a, the multiple peaks at 120–140 ppm of PDI-SiO<sub>2</sub> and PTCDA were C atoms in the conjugated perylene moiety, which caused by the conjugated electrons delocalization in the perylene ring. The carbonyl carbon peak of both PDI-SiO<sub>2</sub> and PTCDA appeared near 160 ppm, while the peak of carbonyl for PDI-SiO<sub>2</sub> was shifted by 3.07 ppm due to the covalent link of SiO<sub>2</sub>. The continuous peaks of 0–50 ppm correspond to the methylene group. Compared with SiO<sub>2</sub>-NH<sub>2</sub>, the chemical shift of methylene in PDI-SiO<sub>2</sub> was reduced by 1.92 ppm due to chemical bonding. The SSNMR results showed that PTCDA was successfully covalently linked to SiO<sub>2</sub> through aminopropyl chain. Fourier-transformed infrared spectrum (FT-IR) further indicated the successful preparation of the PDI-SiO<sub>2</sub>. As shown in Fig. 1b, the peak at 2934  $\text{cm}^{-1}$  of SiO<sub>2</sub>-NH<sub>2</sub> was attributed to the stretching vibration of the amino group, while this characteristic peak disappeared in PDI-SiO<sub>2</sub>, which proved that the condensation reaction between PTCDA and SiO<sub>2</sub>-NH<sub>2</sub> occurred. Moreover, compared with PTCDA, the characteristic peak of C=O at 1760  $\text{cm}^{-1}$  of PDI-SiO<sub>2</sub> was shifted to the low wavenumber, which further confirmed the complete condensation of PTCDA and SiO<sub>2</sub>-NH<sub>2</sub>.

The morphology and structure of PDI-SiO<sub>2</sub> were further investigated. First, the composition and distribution of elements on the surface of PDI-SiO<sub>2</sub> were conducted using X-ray photoelectron spectroscopy (XPS) (Fig. S1) and energy dispersive spectrometer (EDS) (Fig. 1c). Among them, the content of Si on the surface was very low compared with the C and O, indicating that the covalently connected PTCDA was distributed on the external surface of the SiO<sub>2</sub> nanoparticles. Specifically, EDS images can further distinguish the exact regions of PDI and SiO<sub>2</sub>. It can be seen from Fig. S2 that the PDI layer was highly dispersed on the SiO<sub>2</sub> surface with high specific surface area, providing more active sites for the photocatalytic reaction. The isothermal nitrogen adsorption-desorption experiment (Fig. S3) showed that the surface aggregation of PDI was further formed secondary accumulation pores in PDI-SiO<sub>2</sub>. The larger surface area and pore volume of PDI-SiO<sub>2</sub> created more favorable conditions for the activation of PDS and the adsorption degradation of pollutants. Transmission electron microscopy (TEM) images (Fig. 1d) showed that SiO<sub>2</sub>-NH<sub>2</sub> exhibited nanoparticles, while PDI-SiO<sub>2</sub> exhibited particle stacked nanostructure, indicating that covalent bonding did not cause significant differences in morphology. The

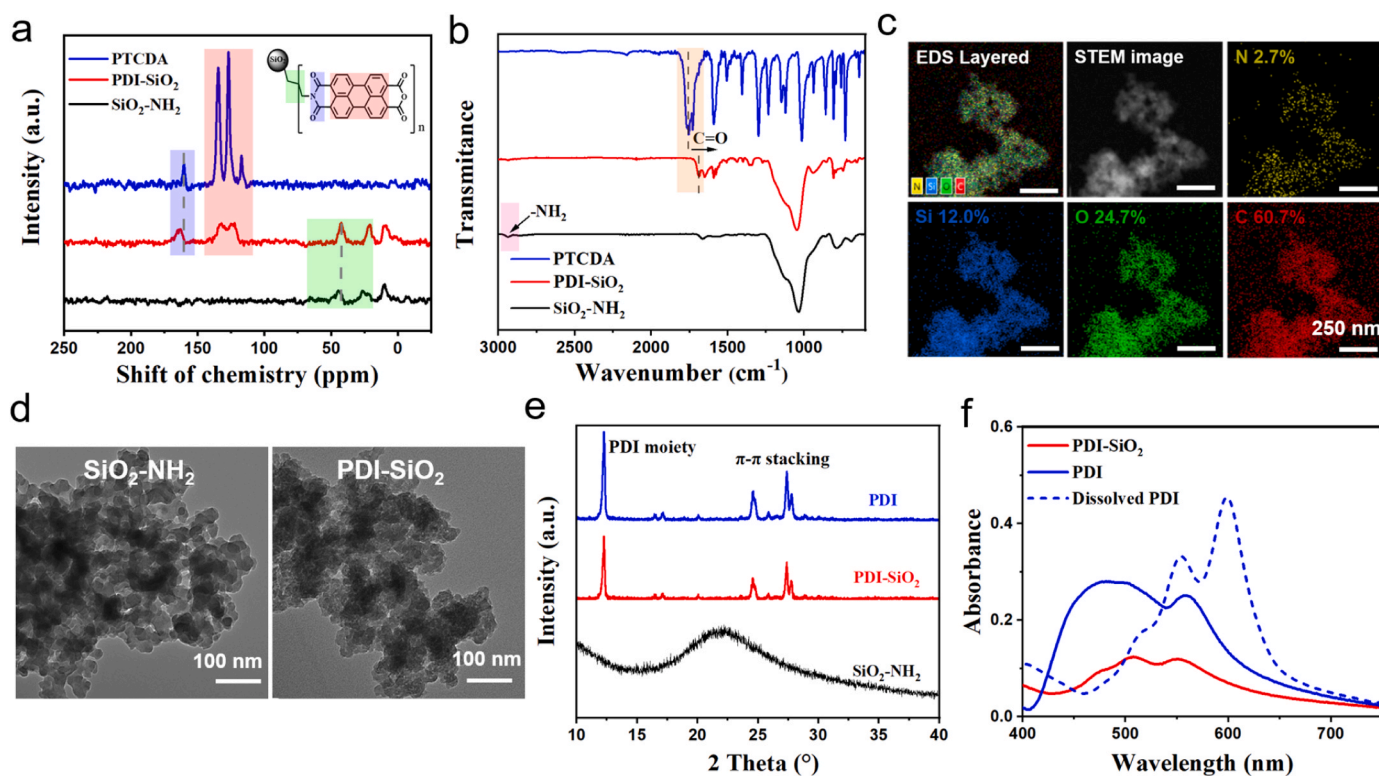


**Fig. 1.** Structure and morphology characterization of PDI-SiO<sub>2</sub>. (a) <sup>13</sup>C solid nuclear magnetic spectra and (b) infrared spectra of PDI-SiO<sub>2</sub>, SiO<sub>2</sub>-NH<sub>2</sub> and PTCDA, (c) EDS images of PDI-SiO<sub>2</sub>. (d) TEM images of SiO<sub>2</sub>-NH<sub>2</sub> and PDI-SiO<sub>2</sub>. (e) XRD pattern of PDI, PDI-SiO<sub>2</sub> and SiO<sub>2</sub>-NH<sub>2</sub>. (f) UV-vis spectra of PDI-SiO<sub>2</sub>, PDI and dissolved PDI.

crystal state of PDI-SiO<sub>2</sub> was characterized by X-ray diffraction (XRD) pattern (Fig. 1e). The characteristic diffraction peaks of PDI and  $\pi$ - $\pi$  stacking appeared in both assembled PDI and PDI-SiO<sub>2</sub> nanoparticles, indicating that PTCDA formed supramolecular structures with small crystal on SiO<sub>2</sub>. Raman spectra further show that PDI-SiO<sub>2</sub> has a lower degree of  $\pi$ - $\pi$  stacking compared to PDI (Fig. S4). Generally,  $\pi$ - $\pi$  stacking interactions in self-assembled supramolecular system can be revealed by UV-vis absorption spectra [44,47]. As shown in Fig. 1f, dissolved PDI (dissolved in H<sub>2</sub>SO<sub>4</sub>) presented two obvious peaks between 550 and 650 nm, while aggregated PDI and PDI-SiO<sub>2</sub> (dispersed in H<sub>2</sub>O) obviously showed the blue shift of maximum absorption peak and the disappearance of fine structure, demonstrating that PDI-SiO<sub>2</sub> was the supermolecule formed by self-assembly through  $\pi$ - $\pi$  stacking (H-aggregate) [48].

### 3.2. Enhanced photogenerated carrier separation of supramolecular PDI-SiO<sub>2</sub>

The photoelectric conversion effect of supramolecular PDI-SiO<sub>2</sub> has been studied. As shown in Fig. 2a, the photocurrent of PDI-SiO<sub>2</sub> under visible light was much stronger than that of PDI, indicating that the short-range crystallization of PDI-SiO<sub>2</sub> can promote carrier separation and transfer effectively. Electrochemical impedance spectroscopy (EIS) further reflected the resistance and photogenerated carrier transport inside the material. Compared with PDI, supramolecular PDI-SiO<sub>2</sub> exhibited the smaller arc radius in Nyquist plots, and the fitted charge transfer resistance  $R_2$  was only 6.9 k $\Omega$  (Fig. 2b), proving the excellent photogenerated carrier separation and transportation in supramolecular PDI-SiO<sub>2</sub>. Furthermore, the photogenerated carrier recombination was investigated. PDI had a strong fluorescence emission signal in the range of 600–800 nm, however, the emission peak decreases significantly after binding with SiO<sub>2</sub> (Fig. 2c), indicating that PDI-SiO<sub>2</sub> complex can promote effective carrier separation.

For a n-type semiconductor, photogenerated electrons and holes would migrate to the bulk and the surface under light irradiation, respectively, thus creating a positive surface photogenerated voltage (SPV) [49]. The stronger SPV signal indicated that more photogenerated holes migrate to the surface, and thus the more efficient separation of photogenerated charge carriers. As PDI a typical n-type semiconductor, PDI-SiO<sub>2</sub> shows a stronger positive SPV response at 350–600 nm (Fig. 2d), indicating that the supramolecular PDI-SiO<sub>2</sub> not only broadens the spectral response range, but also separates more photogenerated holes involved in the oxidation reaction.

The energy band structure of PDI-SiO<sub>2</sub> was further revealed (Fig. S5). The band gap energy of PDI-SiO<sub>2</sub> was calculated to be 1.96 eV through UV-visible diffuse reflectance spectrum (DRS). The Mott-Schottky (MS) curve was measured and the conduction band of PDI-SiO<sub>2</sub> was calculated as  $-0.28$  V. Therefore, the valence band of PDI-SiO<sub>2</sub> was calculated to be 1.68 V. Since the deep valence band position,  $h^+$  generated by PDI-SiO<sub>2</sub> has strong oxidation capacity, which is conducive to the deep mineralization of pollutants.

### 3.3. Photocatalysis promotes PDS activation for bisphenol A degradation

To evaluate the photocatalytic activity of PDI-SiO<sub>2</sub> activated PDS to degrade pollutants, bisphenol A (BPA), a common organic pollutant in wastewater, was selected as the degradation object. Under the condition of light irradiation, PDS alone was relatively stable and could not achieve the degradation of BPA. The introduction of SiO<sub>2</sub> had little changes in activity, while PDI had a certain degree of effect on BPA degradation. Interestingly, BPA was significantly degraded after introduction of PDI-SiO<sub>2</sub> for photocatalytic activation of PDS (Fig. S6). Compared with simulated sunlight (AM 1.5 G), the degradation of BPA under visible light had a higher degradation rate (Fig. 3a), indicating that the material was responsive to visible light and had a higher utilization rate (Fig. S7). Specifically, 10 mg/L of BPA was completely degraded within 30 min



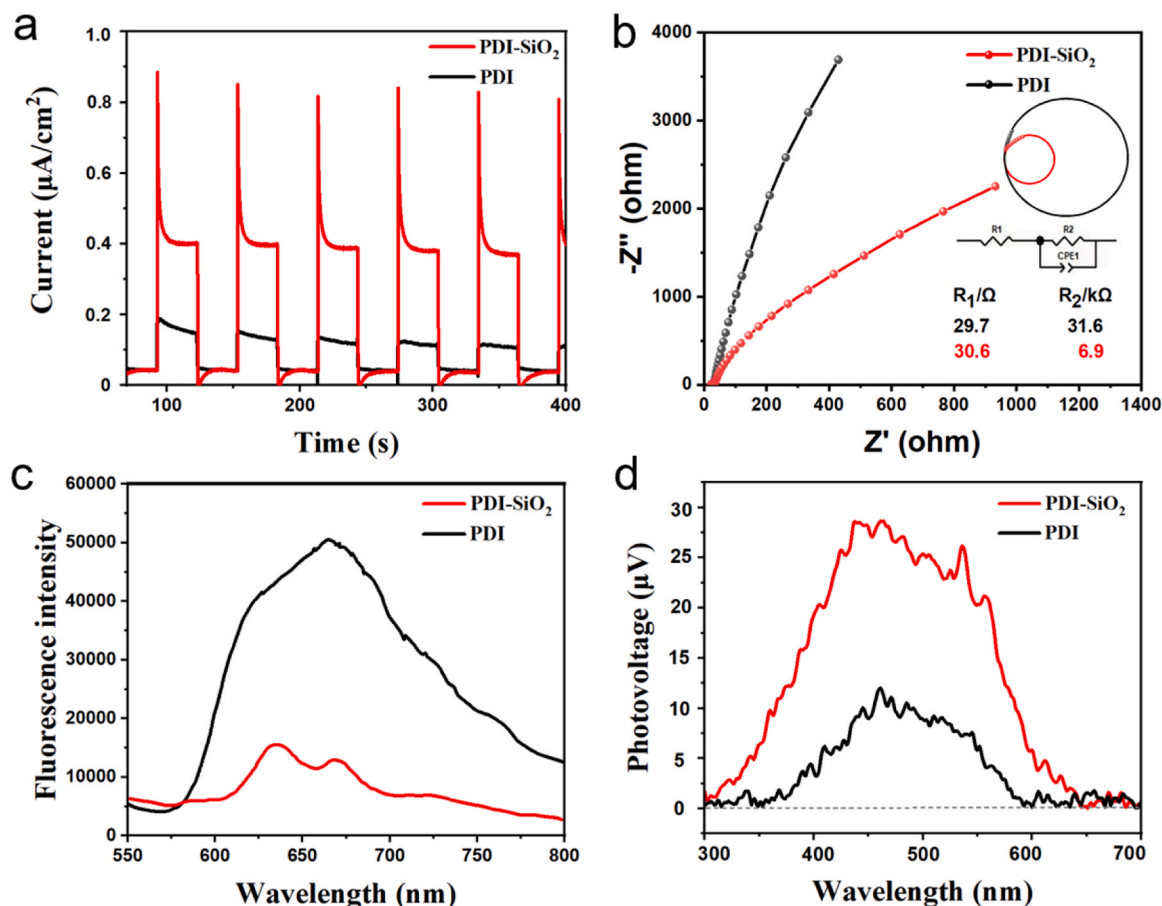


Fig. 2. Photo-electric performance characterization. The contrast between PDI-SiO<sub>2</sub> and PDI in (a) photocurrent; (b) Electrochemical impedance spectra (The illustration is a fitted circle and equivalent circuit diagram, where  $R_1$ ,  $R_2$  and CPE1 represent solution resistance, charge transfer resistance and double layer capacitance); (c) Fluorescence emission spectrum; (d) Surface photovoltage.

under visible light, and the degradation rate constant was as high as  $0.100 \text{ min}^{-1}$ . Next, the cyclic stability of the photocatalytic activation of PDS by PDI-SiO<sub>2</sub> to degrade pollutants was characterized. As shown in Fig. 3b, PDI-SiO<sub>2</sub> maintained stable and high activity in the three cycles of photocatalytic PDS activation for BPA degradation, indicating that PDI-SiO<sub>2</sub> material has excellent reusability. According to the SEM and TEM images of PDI-SiO<sub>2</sub> before and after the cycle (Fig. S8), the structure of PDI-SiO<sub>2</sub> remains stable. In addition, the FT-IR spectrum (Fig. S9) showed that the main characteristic peaks of PDI-SiO<sub>2</sub> had no change before and after cycle, indicating that the main functional groups maintained. The above results show that PDI-SiO<sub>2</sub> has excellent structural stability and high efficiency in the BPA degradation via PDS activation. Compared with common PDI-based self-assembled supramolecular photocatalyst (PDI, PDINH, PDIPA), PDI-SiO<sub>2</sub> exposed more active sites of PDI, which was conducive to the adsorption and enrichment of BPA (Fig. S10), thus exhibiting significantly superior photocatalytic degradation ability after activating PDS (Fig. S11). As shown in Fig. 3c, the mineralization rate of BPA degraded by PDI-SiO<sub>2</sub> + PDS reached 81%, which was at least 40% higher than that of other materials, indicating that it had a good capacity of deep mineralization for BPA.

The photocatalytic advanced oxidation effect of PDI-SiO<sub>2</sub> activated PDS for the degradation of other organic pollutants was studied (Fig. 3d). The photocatalytic activity of PDI-SiO<sub>2</sub> + PDS was evaluated by degradation of phenol, *p*-chlorophenol (4-CP) and 2,4-dichlorophenol (2,4-DCP). The degradation kinetics curves of PDI-SiO<sub>2</sub> for various pollutants show that the degradation of other organic pollutants by PDI-SiO<sub>2</sub> + PDS can be mostly completed within 60 min (Fig. S12). To further

demonstrate the universality of the PDS-activated degradation system, we investigated the degradation performance of PDI-SiO<sub>2</sub> in real water, and analyzed the effects of typical cations and anions in water on degradation rates (Fig. S13).

### 3.4. Mechanism of rapid PDS activation, efficient degradation and deep mineralization

The mechanism of PDS activation by PDI-SiO<sub>2</sub> was studied. The presence of PDI $\cdot^-$  was detected by UV-vis-NIR characteristic absorption [50,51]. As shown in Fig. 4a, in the mixed solution of PDI-SiO<sub>2</sub> and BPA, only the characteristic absorption peak of PDI appears in the visible region in the dark. After 10 min of visible light, the characteristic absorption peaks of PDI $\cdot^-$  appeared at 712 nm, 795 nm and 954 nm, respectively, indicating that PDI-SiO<sub>2</sub> can rapidly consume electrons on BPA to form PDI $\cdot^-$  under visible light. The PDS activation effect can be also reflected by detecting the PDI $\cdot^-$  using electron spin resonance (ESR) [50]. As shown in Fig. 4b, no PDI $\cdot^-$  signal in the aqueous solution of PDI-SiO<sub>2</sub> + BPA in dark. However, it was significantly enhanced after 1 min of light radiation and there was no obvious decline within 20 min ( $g=2.00343$ ), indicating that electrons were steadily accumulated and stored in the form of PDI $\cdot^-$ . It was worth noting that when both BPA and PDS were present in the system, the peak of PDI $\cdot^-$  was drastically quenched under visible light, indicating that PDS can rapidly consume electrons and thus restore PDI $\cdot^-$  to PDI. Therefore, we proposed a PDI $\cdot^-$ -mediated photocatalytic activation process of PDS (Fig. 4c). Under the excitation of visible light, the highly dispersed PDI consumes the surface electrons of BPA and forms PDI $\cdot^-$ . Further, PDS achieves efficient

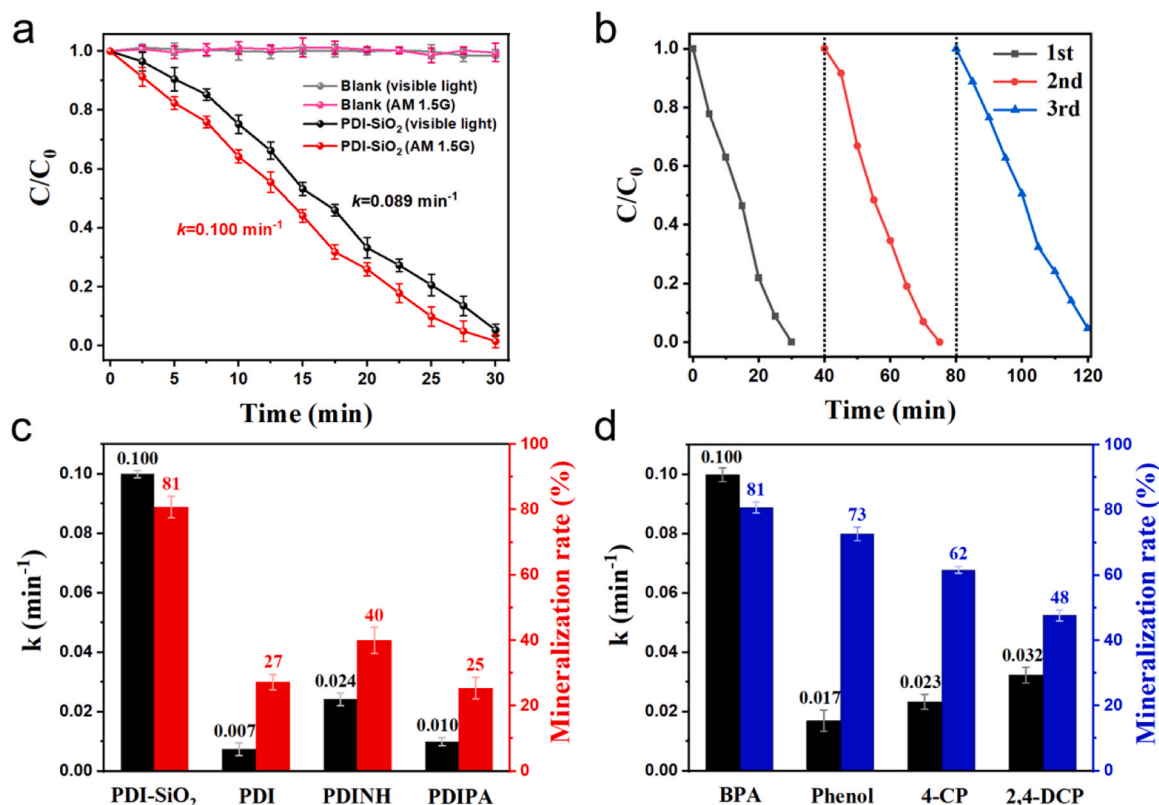


**Fig. 3.** Degradation of organic pollutants of PDI-SiO<sub>2</sub> with PDS activation. (a) The degradation rate of BPA by PDS (1 mM) alone and PDS+PDI-SiO<sub>2</sub> under visible light or simulated sunlight (AM 1.5 G). In the degradation activity test, the BPA concentration was 10 mg/L and the PDI-SiO<sub>2</sub> concentration was 0.5 mg/mL, respectively. (b) Cyclic experiments of BPA degradation by PDS+PDI-SiO<sub>2</sub>. (c) The apparent rate constant and mineralization rate of BPA degradation by PDS with different PDI-based photocatalysts (0.5 mg/mL). (d) Apparent rate constants and mineralization rates of PDS+PDI-SiO<sub>2</sub> degradation for different organic pollutants (10 mg/L).

activation by capturing electrons on PDI<sup>•-</sup>, and this process also greatly promotes the separation and migration of photogenerated holes to the PDI-SiO<sub>2</sub> surface, thus strongly oxidizing pollutants to achieve deep mineralization.

For further understand the mechanism of efficient degradation and deep mineralization, we identified the main active species in the photocatalytic PDS activation through ESR, and further proposed the degradation reaction pathways. Fig. 4d shows the ESR signals of SO<sub>4</sub><sup>•-</sup> and ·OH. There is no obvious signal generation in the PDI-SiO<sub>2</sub> solution system in the dark, and ·OH signals appear after 5 min of irradiation, which is due to the loss of electrons on the hydroxyl group on BPA. After the introduction of PDS and irradiation for 5 min, a significant SO<sub>4</sub><sup>•-</sup> signal appears, which directly proves the activation of PDS. At the same time, SO<sub>4</sub><sup>•-</sup> rapidly oxidize H<sub>2</sub>O, greatly enhancing the ·OH signal. Similarly, Fig. 4e shows the ESR signal for ·O<sub>2</sub>. In the dark, there is no ·O<sub>2</sub> signal in the PDI-SiO<sub>2</sub> system. After 5 min of illumination, the ·O<sub>2</sub> signal appears, which is the result of the interaction between e<sup>-</sup> and O<sub>2</sub>. With the introduction of PDS and light, the ·O<sub>2</sub> signal was significantly enhanced, indicating that the activation of PDS can promote the production of more ·O<sub>2</sub>.

To evaluate the contribution of active oxygen species to pollutant degradation in the process of free radical reaction, we conducted the quenching experiment of active species. Formic acid (HCOOH), methanol (MeOH), *tert*-butanol (t-BuOH), and *p*-benzoquinone (BQ) were used to scavenge h<sup>+</sup>, (·OH and SO<sub>4</sub><sup>•-</sup>), ·OH, ·O<sub>2</sub>, respectively. When different scavengers are added, the degradation rate of the system was suppressed (Fig. S14), thus confirming the presence of the active species. The contribution rates of the above-mentioned active substances in the degradation system are calculated as follows: h<sup>+</sup> was 26.0%, ·OH was 23.0%, SO<sub>4</sub><sup>•-</sup> was 3.0%, and ·O<sub>2</sub> was 44.0% (Fig. 4f). Among them, ·O<sub>2</sub>

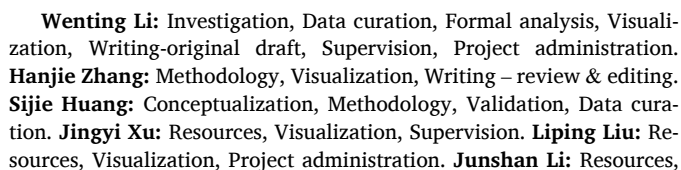
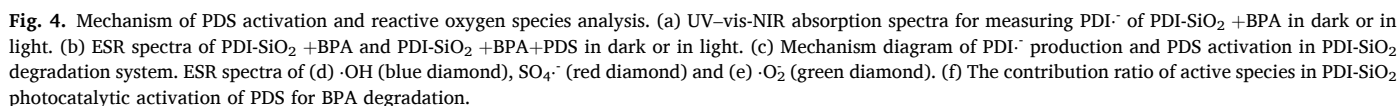
was the main active species, and thus the effect of solvent oxygen on the degradation rate was further studied (Fig. S15). The contribution of SO<sub>4</sub><sup>•-</sup> and ·OH produced by PDS activation is almost the same as that of the strongly oxidizing h<sup>+</sup>.

In this case, we proposed the mechanism of PDI-SiO<sub>2</sub> activated PDS (Fig. 5). Under the visible light, photogenerated holes (h<sup>+</sup>) and electrons (e<sup>-</sup>) generated and migrated to the PDI-SiO<sub>2</sub> surface. Among them, h<sup>+</sup> can directly oxidize pollutants to achieve degradation, and it can also oxidize H<sub>2</sub>O to generate ·OH. e<sup>-</sup> combines with PDI to form PDI<sup>•-</sup>. On the one hand, PDI<sup>•-</sup> reacts with O<sub>2</sub> to form ·O<sub>2</sub>, which reacted with PDS to form SO<sub>4</sub><sup>•-</sup>. On the other hand, when PDI<sup>•-</sup> activates PDS to form SO<sub>4</sub><sup>•-</sup>, which further reacts with H<sub>2</sub>O to form more ·OH.

Finally, the structure-activity relationship between PDI-SiO<sub>2</sub> photocatalyst and PDS activation was summarized. The microcrystalline supramolecular structure of PDI-SiO<sub>2</sub> enhanced photogenerated carrier separation and migration. Moreover, the highly dispersed PDI effectively combined with PDS and pollutants to generate a variety of reactive species for efficient degradation and deep mineralization.

#### 4. Conclusions

In summary, an electron-enriched supramolecular PDI-SiO<sub>2</sub> was designed to promote PDS activation and photogenerated hole migration for enhancing photocatalytic advanced oxidation of organic pollutants. Highly dispersed PDI enhanced the adsorption of pollutants and PDS while generating electron-enriched PDI<sup>•-</sup> for rapid activation of PDS, thus accelerating the degradation of BPA via the production of plentiful h<sup>+</sup>, SO<sub>4</sub><sup>•-</sup>, ·OH, and ·O<sub>2</sub>. Furthermore, photocatalytic-assisted PDS activation promoted charge separation and migration in supramolecular PDI-SiO<sub>2</sub>, resulting in highly efficient organic contaminant degradation



Supplementary data associated with this article can be found in the online version at [doi:10.1016/j.apcatb.2023.123262](https://doi.org/10.1016/j.apcatb.2023.123262).



## References

- [1] J.L. Wang, S.Z. Wang, Activation of persulfate (PS) and peroxymonosulfate (PMS) and application for the degradation of emerging contaminants, *Chem. Eng. J.* 334 (2018) 1502–1517.
- [2] H.V. Lutze, S. Bircher, I. Rapp, N. Kerlin, R. Bakkour, M. Geisler, C. von Sonntag, T. C. Schmidt, Degradation of chlorotriazine pesticides by sulfate radicals and the influence of organic matter, *Environ. Sci. Technol.* 49 (2015) 1673–1680.
- [3] W.D. Oh, Z.L. Dong, T.T. Lim, Generation of sulfate radical through heterogeneous catalysis for organic contaminants removal: current development, challenges and prospects, *Appl. Catal. B: Environ.* 194 (2016) 169–201.
- [4] S. Wacławek, H.V. Lutze, K. Grubel, V.V.T. Padil, M. Cernik, D.D. Dionysiou, Chemistry of persulfates in water and wastewater treatment: a review, *Chem. Eng. J.* 330 (2017) 44–62.
- [5] A.D. Bokare, W. Choi, Review of iron-free Fenton-like systems for activating  $H_2O_2$  in advanced oxidation processes, *J. Hazard. Mater.* 275 (2014) 121–135.
- [6] A. Ghauch, A. Tuqan, Oxidation of bisoprolol in heated persulfate/ $H_2O$  systems: kinetics and products, *Chem. Eng. J.* 183 (2012) 162–171.
- [7] G.P. Anipsitakis, D.D. Dionysiou, Radical generation by the interaction of transition metals with common oxidants, *Environ. Sci. Technol.* 38 (2004) 3705–3712.
- [8] X.X. He, A.A. de la Cruz, D.D. Dionysiou, Destruction of cyanobacterial toxin cylindrospermopsin by hydroxyl radicals and sulfate radicals using UV-254 nm activation of hydrogen peroxide, persulfate and peroxymonosulfate, *J. Photoch. Photobio. A* 251 (2013) 160–166.
- [9] M.M. Ahmed, S. Barbati, P. Doumenq, S. Chiron, Sulfate radical anion oxidation of diclofenac and sulfamethoxazole for water decontamination, *Chem. Eng. J.* 197 (2012) 440–447.
- [10] I.A. Ike, K.G. Linden, J.D. Orbell, M. Duke, Critical review of the science and sustainability of persulfate advanced oxidation processes, *Chem. Eng. J.* 338 (2018) 651–669.
- [11] C. Luo, J. Ma, J. Jiang, Y. Liu, Y. Song, Y. Yang, Y. Guan, D. Wu, Simulation and comparative study on the oxidation kinetics of atrazine by UV/ $H_2O_2$ , UV/ $H_2SO_5$  and UV/ $S_2O_8^{2-}$ , *Water Res.* 80 (2015) 99–108.
- [12] Y.Y. Ahn, E.T. Yun, J.W. Seo, C. Lee, S.H. Kim, J.H. Kim, J. Lee, Activation of peroxymonosulfate by surface-loaded noble metal nanoparticles for oxidative degradation of organic compounds, *Environ. Sci. Technol.* 50 (2016) 10187–10197.
- [13] P. Devi, U. Das, A.K. Dalai, In-situ chemical oxidation: principle and applications of peroxide and persulfate treatments in wastewater systems, *Sci. Total Environ.* 571 (2016) 643–657.
- [14] T. Chaoqun, N.-Y. Gao, Y. Deng, N. An, J. Deng, Heat-activated persulfate oxidation of diuron in water, *Chem. Eng. J.* 203 (2012) 294–300.
- [15] J.F. Yang, L. Yang, Z.S. Bai, L. Ou, C.B. Liu, L.Y. Zheng, Y.F. Yang, G.G. Ying, S. L. Luo, Degradation of azole fungicide fluconazole in aqueous solution by thermally activated persulfate, *Chem. Eng. J.* 321 (2017) 113–122.
- [16] X. Lou, C. Fang, Z. Geng, Y. Jin, D. Xiao, Z. Wang, J. Liu, Y. Guo, Significantly enhanced base activation of peroxymonosulfate by polyphosphates: kinetics and mechanism, *Chemosphere* 173 (2017) 529–534.
- [17] H. Peng, L. Xu, W. Zhang, F. Liu, X. Lu, W. Lu, M. Danish, K. Lin, Different kinds of persulfate activation with base for the oxidation and mechanism of BDE209 in a spiked soil system, *Sci. Total Environ.* 574 (2017) 307–313.
- [18] L. Bu, S. Zhou, Z. Shi, L. Deng, G. Li, Q. Yi, N. Gao, Degradation of oxcabazepine by UV-activated persulfate oxidation: kinetics, mechanisms, and pathways, *Environ. Sci. Pollut. Res.* 23 (2016) 2848–2855.
- [19] Y. Xiao, L. Zhang, W. Zhang, K.Y. Lim, R.D. Webster, T.T. Lim, Comparative evaluation of iodoacids removal by UV/persulfate and UV/ $H_2O_2$  processes, *Water Res.* 102 (2016) 629–639.
- [20] A. Ghauch, A. Baalbaki, M. Amasha, R. El Asmar, O. Tantawi, Contribution of persulfate in UV-254 nm activated systems for complete degradation of chloramphenicol antibiotic in water, *Chem. Eng. J.* 317 (2017) 1012–1025.
- [21] L. Hu, X. Yang, S. Dang, An easily recyclable Co/SBA-15 catalyst: heterogeneous activation of peroxymonosulfate for the degradation of phenol in water, *Appl. Catal. B: Environ.* 102 (2011) 19–26.
- [22] F. Chi, B. Song, B. Yang, Y. Lv, S. Ran, Q. Huo, Activation of peroxymonosulfate by BiFeO<sub>3</sub> microsphere under visible light irradiation for decomposition of organic pollutants, *RSC Adv.* 5 (2015) 67412–67417.
- [23] Y.B. Wang, X. Zhao, D. Cao, Y. Wang, Y.F. Zhu, Peroxymonosulfate enhanced visible light photocatalytic degradation bisphenol A by single-atom dispersed Ag mesoporous g-C<sub>3</sub>N<sub>4</sub> hybrid, *Appl. Catal. B: Environ.* 211 (2017) 79–88.
- [24] J.J. Zhang, X. Zhao, Y.B. Wang, Y. Gong, D. Cao, M. Qiao, Peroxymonosulfate-enhanced visible light photocatalytic degradation of bisphenol A by perylene imide-modified g-C<sub>3</sub>N<sub>4</sub>, *Appl. Catal. B: Environ.* 237 (2018) 976–985.
- [25] S.D. Yan, Y. Shi, Y.F. Tao, H. Zhang, Enhanced persulfate-mediated photocatalytic oxidation of bisphenol A using bioelectricity and a g-C<sub>3</sub>N<sub>4</sub>/Fe<sub>2</sub>O<sub>3</sub> heterojunction, *Chem. Eng. J.* 359 (2019) 933–943.
- [26] L. Yang, X. Bai, J. Shi, X.Y. Du, L. Xu, P.K. Jin, Quasi-full-visible-light absorption by D35-TiO<sub>2</sub>/g-C<sub>3</sub>N<sub>4</sub> for synergistic persulfate activation towards efficient photodegradation of micropollutants, *Appl. Catal. B: Environ.* 256 (2019), 117759.
- [27] Y. Shi, J. Li, D. Wan, J. Huang, Y. Liu, Peroxymonosulfate-enhanced photocatalysis by carbonyl-modified g-C<sub>3</sub>N<sub>4</sub> for effective degradation of the tetracycline hydrochloride, *Sci. Total Environ.* 749 (2020), 142313.
- [28] H. Miao, J. Yang, Y.Q. Sheng, W.L. Li, Y.F. Zhu, Controlled synthesis of higher interfacial electron transfer graphite-like carbon nitride/perylene-tetracarboxylic diimide heterogeneous for enhanced photocatalytic activity, *Sol. Rrl.* 5 (2021) 2000453.
- [29] Y. Wang, H. Wang, J. Li, X. Zhao, Facile synthesis of metal free perylene imide-carbon nitride membranes for efficient photocatalytic degradation of organic pollutants in the presence of peroxymonosulfate, *Appl. Catal. B: Environ.* 278 (2020) 18981.
- [30] Q.Y. Ji, X.Y. Cheng, Y.J. Wu, W.M. Xiang, H. He, Z. Xu, C.M. Xu, C.D. Qi, S.Y. Li, L. M. Zhang, S.G. Yang, Visible light absorption by perylene diimide for synergistic persulfate activation towards efficient photodegradation of bisphenol A, *Appl. Catal. B: Environ.* 282 (2021), 119579.
- [31] H.J. Zhang, X.J. Chen, Z.J. Zhang, K.Y. Yu, W. Zhu, Y.F. Zhu, Highly-crystalline triazine-PDI polymer with an enhanced built-in electric field for full-spectrum photocatalytic phenol mineralization, *Appl. Catal. B: Environ.* 287 (2021), 119957.
- [32] J. Yang, H. Miao, W.L. Li, H.Q. Li, Y.F. Zhu, Designed synthesis of a p-Ag<sub>2</sub>S/n-PDI self-assembled supramolecular heterojunction for enhanced full-spectrum photocatalytic activity, *J. Mater. Chem. A* 7 (2019) 6482–6490.
- [33] P. Garg, S. Kumar, I. Choudhuri, A. Mahata, B. Pathak, Hexagonal planar CdS monolayer sheet for visible light photocatalysis, *J. Phys. Chem. C* 120 (2016) 7052–7060.
- [34] S. Dutta, S. Chatterjee, I. Mukherjee, R. Saha, B.P. Singh, Fabrication of ZnS hollow spheres and RGO-ZnS nanocomposite using cysteamine as novel sulfur source: Photocatalytic performance on industrial dyes and effluent, *Ind. Eng. Chem. Res.* 56 (2017) 4768–4778.
- [35] D. Wang, L. Huang, Z. Guo, S. Jin, C. Liu, W. Wang, W. Yuan, Efficient heterojunctions via the in-situ self-assembly of BiVO<sub>4</sub> quantum dots on SiC facets for enhanced photocatalysis, *ACS Appl. Nano Mater.* 1 (2018) 4594–4601.
- [36] C. Wu, J. Zhang, X. Tong, P. Yu, J.Y. Xu, J. Wu, Z.M. Wang, J. Lou, Y.L. Chueh, A critical review on enhancement of photocatalytic hydrogen production by molybdenum disulfide: From growth to interfacial activities, *Small* 15 (2019), e1900578.
- [37] D.D. Zhu, Q.X. Zhou, Novel Bi<sub>2</sub>WO<sub>6</sub> modified by N-doped graphitic carbon nitride photocatalyst for efficient photocatalytic degradation of phenol under visible light, *Appl. Catal. B: Environ.* 268 (2020), 118426.
- [38] Y. Zhang, J.B. Zhou, X. Chen, L. Wang, W.Q. Cai, Coupling of heterogeneous advanced oxidation processes and photocatalysis in efficient degradation of tetracycline hydrochloride by Fe-based MOFs: Synergistic effect and degradation pathway, *Chem. Eng. J.* 369 (2019) 745–757.
- [39] A. Nagai, X. Chen, X. Peng, X.S. Ding, Z.Q. Guo, D.L. Jiang, A squaraine-linked mesoporous covalent organic framework, *Angew. Chem. Int. Ed.* 52 (2013) 3770–3774.
- [40] Z.J. Wang, X.Y. Yang, T.J. Yang, Y.B. Zhao, F. Wang, Y. Chen, J.H. Zeng, C. Yan, F. Huang, J.X. Jiang, Dibenzothiophene dioxide based conjugated microporous polymers for visible-light-driven hydrogen production, *ACS Catal.* 8 (2018) 8590.
- [41] K. Kumar, S. Kaur, S. Kaur, G. Bhargava, S. Kumar, P. Singh, Self-assembled nanofibers of perylene diimide for the detection of hypochlorite in water, bio-fluids and solid-state: exogenous and endogenous bioimaging of hypochlorite in cells, *J. Mater. Chem. B* 8 (2020) 125–135.
- [42] W. Liu, C. He, S. Huang, K. Zhang, W. Zhu, L. Liu, Z. Zhang, E. Zhu, Y. Chen, C. Chen, Y. Zhu, Enhancing carrier transport via  $\sigma$ -linkage length modulation in D- $\sigma$ -A semiconductors for photocatalytic oxidation, *Angew. Chem. Int. Ed.* (2023), e202304773.
- [43] J.T. Shang, H.Y. Tang, H.W. Ji, W.H. Ma, C.C. Chen, J.C. Zhao, Synthesis, characterization, and activity of a covalently anchored heterogeneous perylene diimide photocatalyst, *Chin. J. Catal.* 38 (2017) 2094–2101.
- [44] D. Liu, J. Wang, X. Bai, R. Zong, Y. Zhu, Self-assembled PDINH supramolecular system for photocatalysis under visible light, *Adv. Mater.* 28 (2016) 7284–7290.
- [45] A. Datar, K. Balakrishnan, L. Zang, One-dimensional self-assembly of a water soluble perylene diimide molecule by pH triggered hydrogelation, *Chem. Commun.* 49 (2013) 6894–6896.
- [46] Z. Zhang, J. Wang, D. Liu, W. Luo, M. Zhang, W. Jiang, Y. Zhu, Highly efficient organic photocatalyst with full visible light spectrum through  $\pi$ - $\pi$  stacking of TCNQ-PTCDI, *ACS Appl. Mater. Interfaces* 8 (2016) 30225–30231.
- [47] J. Wang, D. Liu, Y.F. Zhu, S.Y. Zhou, S.Y. Guan, Supramolecular packing dominant photocatalytic oxidation and anticancer performance of PDI, *Appl. Catal. B: Environ.* 231 (2018) 251–261.
- [48] R.X. Niu, C.J. Pan, Z.M. Chen, L.H. Wang, L. Wang, Enhanced thermoelectric performance from self-assembled alkyl chain-linked naphthalenediimide/single walled carbon nanotubes composites, *Chem. Eng. J.* 381 (2020), 122650.
- [49] R.T. Chen, F.T. Fan, T. Dittrich, C. Li, Imaging photogenerated charge carriers on surfaces and interfaces of photocatalysts with surface photovoltage microscopy, *Chem. Soc. Rev.* 47 (2018) 8238–8262.
- [50] X. Yang, Y. Li, G.Y. Chen, H.R. Liu, L. Li Yuan, L. Yang, D. Liu, ZnSnO<sub>3</sub> quantum dot/perylene diimide supramolecular nanorod heterojunction photocatalyst for efficient phenol degradation, *ACS Appl. Nano Mater.* 5 (2022) 9829–9839.
- [51] I. Ghosh, T. Ghosh, J.I. Bardagi, B. Konig, Reduction of aryl halides by consecutive visible light-induced electron transfer processes, *Science* 346 (2014) 725–728.